

Instrumentation and Diagnosis on a Vacuum Pump

ARPE Project

Anne COULON¹, Renaud BERTONI¹

¹VIBRATEC

28, chemin du petit bois, 69130 Ecully, France
{renaud.bertoni}@vibratec.fr

Abstract

The ARPE project is a collaborative project in which Vibratec is involved, aiming to bring significant improvement to noise reduction and multiphysics modelling of Roots pumps.

As part of this project, a measurement campaign performed on six different pumps has highlighted significant noise level differences between them, as well as noise perception discrepancies. A psychoacoustic criterion has therefore been constructed to sort the pumps.

The vibroacoustic diagnosis showed that the presence of contact loss in the gear is responsible for the acoustic perception differences. In addition to this, different vibro-impact regimes have been identified.

ARPE project is ongoing; the focus will now be put on the identification of the parameters responsible for the vibro-impact regime appearance and transitions. The aim is to construct a relationship between these parameters and the psychoacoustic criterion.

1 Introduction

The noise radiated by Roots type vacuum pumps is a major drawback that jeopardizes their utilization. The noise sources and the mechanisms acting in this type of pump are complex, strongly coupled, and their modelling is not yet mastered.

The ARPE project (Acoustique et vibRation des Pompes à vidE) is a collaborative project in which Vibratec is involved. Its aim is to bring significant improvement to noise reduction and multiphysics modelling of Roots pumps. Indeed, this project includes 3D fluid calculations in a chamber whose geometry is constantly changing, coupled with nonlinear dynamic calculation of the gear meshing process. The previous computations are finally integrated in a global numerical vibro-acoustic model.

The complexity of the task requires a measurement campaign, set up to:

- a. Provide input and tune numerical models with static and dynamic pressure, temperature, vibration, rotation speed and torque data;
- b. Diagnose the pumps: find noise indicators in order to differentiate the pumps' acoustic performances, find the vibro-acoustic radiation mechanisms, link the perceived noise and the pumps' vibro-acoustic behavior.

In this paper, the instrumentation (incremental encoders, dynamic pressure sensors inside the chamber, indirect torque measurements) and the difficulties encountered to set it up (vacuum problems, small space, sensitivity of the structure) are presented. Then, the data post-processing is detailed, from the simple noise level comparison to the transmission path analysis.

2 General experimental set-up

2.1 Studied elements

Six specimens of the same multistage vacuum pump model were studied during this project. The pumps 1, 3 and 5 are equivalent in terms of drive, motor, and lobe alignment. Other pumps (2, 6-A and 6-B) differ by their lobe alignments, their motors (asynchronous / synchronous) and/or their drives (see Table 1).

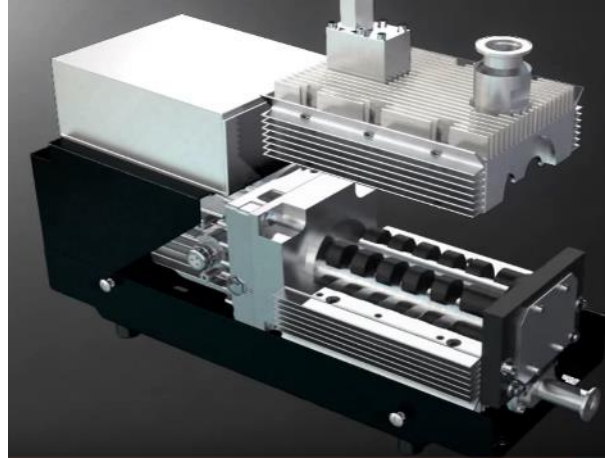


Figure 1: Illustration of the internal arrangement of a multi-stage vacuum pump

Pump n°	Configuration (motor, drive, internal alignment)
1	A
2	B
3	A
5	A
6-A	C
6-B	D

Table 1: Tested pumps and corresponding configurations

From a kinematic point of view, the pumps run at 6000 rpm with a timing gear composed of two pinions with 38 teeth each. Each pump is composed of 6 pressure stages.

Fluid pulsation is expected at harmonics H4 (400 Hz) and H8 (800 Hz) of the rotation frequency.

2.2 Instrumentation

2.2.1 Foreword

The measurement campaign was led not only to understand the pump vibro-acoustic behavior, but also to feed the multiphysics numerical models. Several physical quantities were consequently required, involving an extensive instrumentation. This instrumentation was defined to avoid any perturbation of the pump dynamic behavior, increasing its complexity: the vacuum must be maintained, gas flow must not be modified (turbulences) and the pump's structure must be preserved as much as possible. All the measurements are detailed hereafter.

2.2.1 Torque measurements

The pump torque measurements are a good example of the instrumentation's complexity: in stabilized operating conditions, the estimated torque corresponds to a 5 $\mu\text{m/m}$ shaft strain, which is not easily measurable.

Measuring the torque by an extensometry method [1] would imply the replacement of the actual shaft by a hollow, more elastic, one. This would change the line's dynamic response and the hollow shaft needed to

obtain a sufficient signal/noise ratio would be very fragile. Moreover, a sealed slip ring would be necessary to transmit the signal while maintaining the vacuum.

Considering this mounting fragility/complexity, it was decided to perform an indirect torque measurement. To do so, the motors were characterized on a test bench to determine the following relations:

$$torque = f(current) \quad (1)$$

$$torque = f(rotationspeed) \quad (2)$$

Thus, in operating conditions, the current and speed measurements enable the calculation of the corresponding torque according to the relations (1) and (2).

2.2.2 Pressure measurements

Static and dynamic pressures were measured in the inter-stage cavities (see Figure 4 and Figure 5). Specific supports were designed to avoid gas leaks and to ensure flush sensor mounting.

2.2.3 Temperature measurements

Temperature measurement is essential to tune the 3D fluid model and also to ensure that all measurements performed on the pumps are made in the same stabilized operating conditions. Moreover, temperature can be an indicator of the dynamic behavior difference between the pumps. For that purpose, 7 thermocouples were inserted inside the upper and lower shells (see Figure 5) and one was set up inside the oil tank. In addition, temperature was measured inside the interstage cavities.

2.2.4 Speed measurements

The average speed was obtained by the use of an eddy current sensor aiming at the leading gear (see Figure 2 and Figure 5).

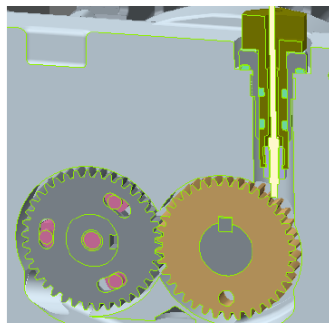


Figure 2: Eddy current sensor mounting

Two optical encoders (1000 i/r) were mounted at the end of the two shafts, on the low-pressure side. A specific mounting was designed to ensure the encoder adjustment. The housing was extended to maintain the vacuum (see Figure 3). These encoders were combined with a high sampling rate acquisition card, which makes it possible to obtain each shaft's instantaneous rotation speed. It was then possible to calculate the speed difference between the shafts and visualize potential contact loss at the pinion teeth.

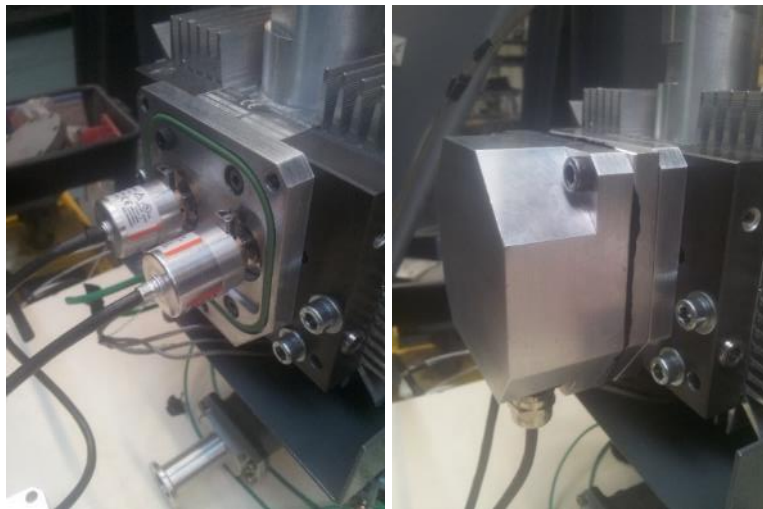


Figure 3: Optical encoder mounting

2.2.5 Noise and vibration measurements

A set of five microphones were located at 1 m from side of the pump, making it possible to estimate the sound power level. Also, a tri-axial accelerometer was glued to the gear housing and another one to the low-pressure bearing housing (see Figure 4).

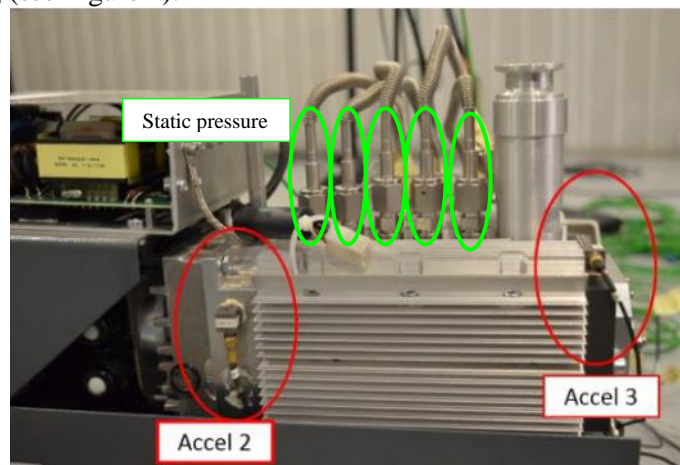


Figure 4: Instrumentation: accelerometers (red circles) and static pressure sensors (green circles)

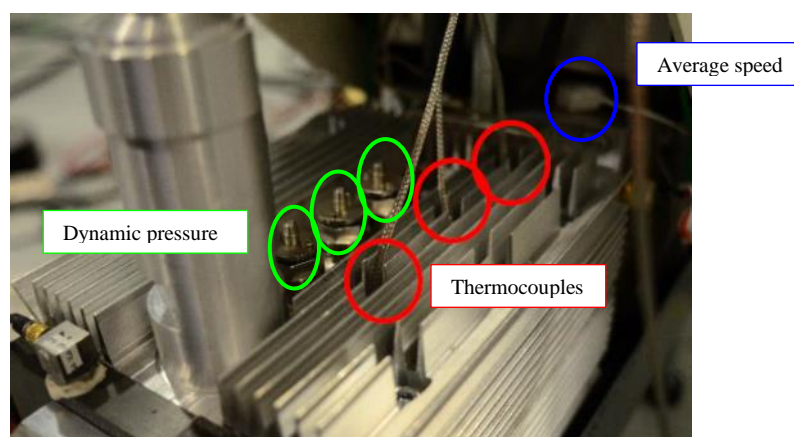


Figure 5: Instrumentation: thermocouples (red circles) and dynamic pressure sensors (green circles) average speed: Eddy current sensor (blue circle)

2.3 Test conditions

Four flow configurations were tested, from no load (pump exhaust under vacuum) to 30 SLM load (30 standard liters pumped per minute).

The diagnosis presented hereafter only deals with the “limit pressure” state. In this configuration, the pump intake pipe was blocked, meaning that in stabilized operating conditions, the first stage was under vacuum while last stage was at atmospheric pressure.

Measurements were performed in a semi-anechoic room, with the pumps started 4 hours before the tests to ensure their thermal stability. Each measurement was reproduced at least 3 times.

3 Measurement results

3.1 Finding an acoustic criterion

Figure 6 illustrates the spectral content of the pumps 1, 3 and 5; two main noise areas appear on these third octave spectra: [630-1000] Hz and [2500-5000] Hz. The third octave band 800 Hz is the most energetic. Sound pressure levels can differ by 6 dB from one pump to another.

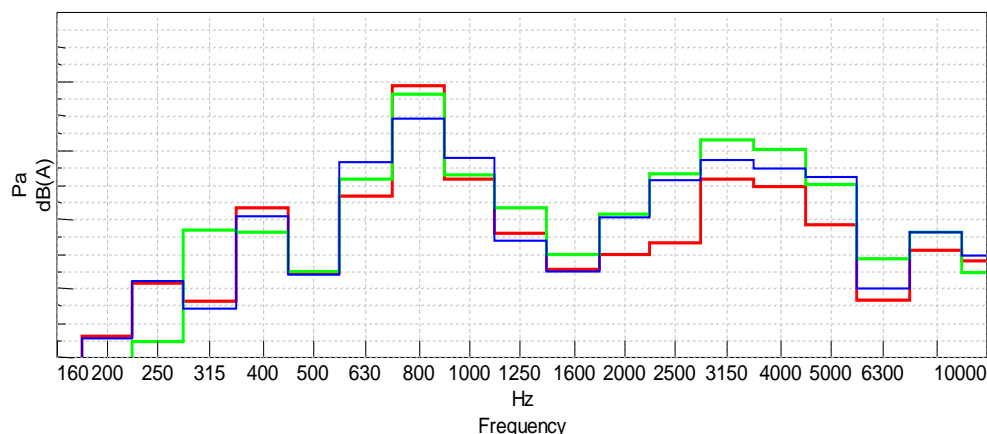


Figure 6: Third octave sound pressure levels
red: Pump 1 - green: pump3 - blue: Pump 5 - scale: 2.5dB/step

The ARPE project aims to improve the pumps acoustic perception; thus, a psycho- acoustic listening test was set up to discriminate the sounds emitted by the six pumps. The results of this test, presented Figure 7, indicate that the Pump 1 was largely preferred to the others, whereas pump 2 is the most disruptive.

Also, the comparison of pumps 1, 3 and 5 reveals an important deviation between those three pumps, which have the same design: Pump 1 is liked for its stable noise, in opposition to Pump 3, more instable and presenting an additional noise signature that can be interpreted as rattle noise, appearing and disappearing. Pump 5 is noisier than the Pump 1, but is more unsettling (see Table 2). This is probably due to its noise modulation, compared to Pump 1's stability.

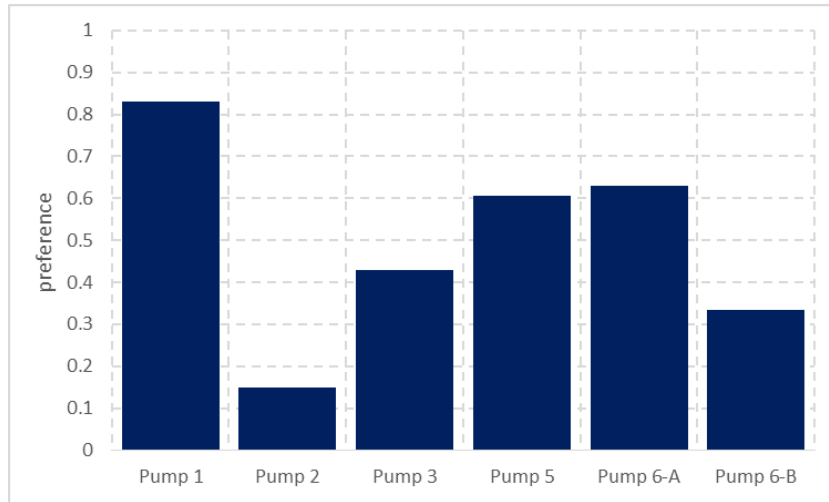


Figure 7: Psychoacoustic classification of the pumps

The classification issued from the global sound pressure level comparison differs significantly from the preference test classification (see Table 2).

In order to link the subjective noise perception to a physical quantity, a combined criterion was constructed taking account of the several psychoacoustic indicators. This criterion provides good correlation with the psychoacoustic classification (Figure 8): the pumps can be sorted with a single sound pressure measurement.

For confidential matters, the criterion details cannot be provided in this paper. A simple explanation is that a pump with a combined criterion close to 1 presents an annoyance level close to that of Pump 1. The higher the combined criterion, the more disturbing the pump.

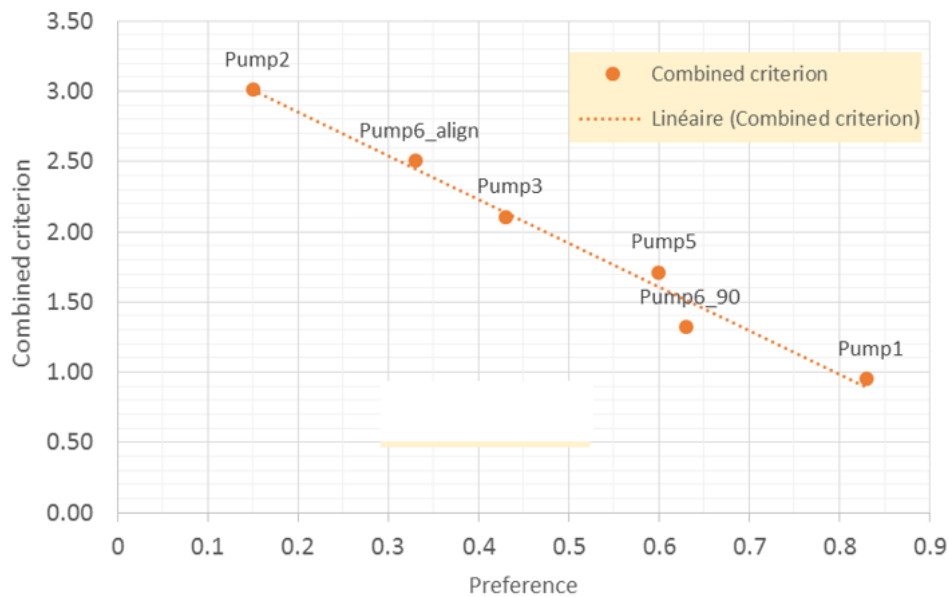


Figure 8: Combined Criterion vs. preference

Though it is useful to sort the pumps, the combined criterion does not provide any information that can explain the perception difference between the pumps 1, 3 and 5, while they have the same design. The vibro-acoustic diagnosis presented in the following section focuses on these pumps.

	Sound Level classification		Psychoacoustic classification
<i>Best pump</i>	Pump 6-90		Pump 1
	Pump 5	(+ 2.0 dB)	Pump 6-90
	Pump 6-align	(+ 2.8 dB)	Pump 5
	Pump 1	(+ 3.3 dB)	Pump 3
	Pump 3	(+ 5 dB)	Pump 6-align
<i>Worst pump</i>	Pump 2	(+ 6.5 dB)	Pump 2

Table 2: Sound level and psychoacoustic classification

3.2 Comparison between the pumps presenting the same design

A first approach consisted in comparing macroscopic indicators such as the pressure pulsation, the sound power or the torque. Table 3 summarizes the results. In this table, measurements of pumps 3 and 5 are compared to Pump 1 values, used as a reference.

	Sound power level (dB(A) ref. 1pW)	Nominal torque (N.m)	Pulsation level Stage 4 (mbar Peak-peak)	Pulsation level Stage 5 (mbar Peak-peak)	Pulsation level Stage 6 (mbar Peak-peak)
<i>Pump 1</i>	Reference	Reference	Reference	Reference	Reference
<i>Pump 3</i>	+1.7 dB	- 6 %	- 9%	+ 2 %	+ 17 %
<i>Pump 5</i>	-1.3 dB	- 2 %	- 6%	+ 15 %	+ 26 %

Table 3: Global indicators: sound power level, average torque, pressure pulsation

The average torque delivered by the motors is homogenous, meaning that the braking torque due to lubrication and friction is equivalent for the three pumps. This statement is confirmed by measurements performed in no load conditions (not presented here).

The dynamic pressure pulsations of pumps 3 and 5 increase at the exhaust, without any correlation with the noise level. It is important to keep in mind that pressure pulsation order of magnitude is around 100 mbar, which means that a 25 % difference corresponds roughly to 25 mbar.

Figure 9 to Figure 11 present the angle domain order spectra calculated for the pumps 1, 3 and 5. Using the angle domain makes it possible to reduce the measurement noise and focus on the synchronous phenomena. In addition, speed fluctuations that can pollute the spectra high-frequency content are avoided.

On each figure, the top spectrum corresponds to the sound pressure level at 1 m above the pump (microphone 5), while the bottom plots displays the gear housing accelerometer spectra and the internal dynamic pressure spectra at the exhaust stage.

Lateral bands around the rotation frequency and kinematic frequencies are observed on each one of the three plots. At the exhaust stage, pressure spectra are equivalent in terms of content and trend for all pumps, and are therefore not related to the noise differences: the fluid excitation is equivalent for all pumps.

The acoustic spectrum of Pump 3 is richer than Pump 1's around the third order and in the order 8 to order 13 range. In this range, an amplification appears each $\frac{1}{2}$ order, modulated by the asynchronous motor slip frequency. This phenomenon is also visible on the accelerometer spectrum, which is 5 to 10 times higher than Pump 1's between orders 3 and 15.

A possible explanation for this slip frequency modulation is the presence of a motor static and dynamic eccentricity, either due to the fitting clearance or to a modal appropriation of the shaft bending modes including a rotor participation.

Pump 5's noise and vibration spectra are closer to Pump 1's than to Pump 3's: they are mainly constituted of harmonics. Pump 3's vibration spectrum is most representative of a random shock response spectrum added to the forced excitation spectrum. Half harmonics point out a periodic unbalance excitation linked either to a bending or a shock.



Figure 9: Order spectrum (Δ order = 0.01); Pump 1
 Top: Microphone 5 (scale: 5 dB/div)
 Bottom: Gear housing accelerometer (red); dynamic pressure stage 6 (green)



Figure 10: Order spectrum (Δ order = 0.01); Pump 3
 Top: Microphone 5 (scale: 5 dB/div)
 Bottom: Gear housing accelerometer (red); dynamic pressure stage 6 (green)

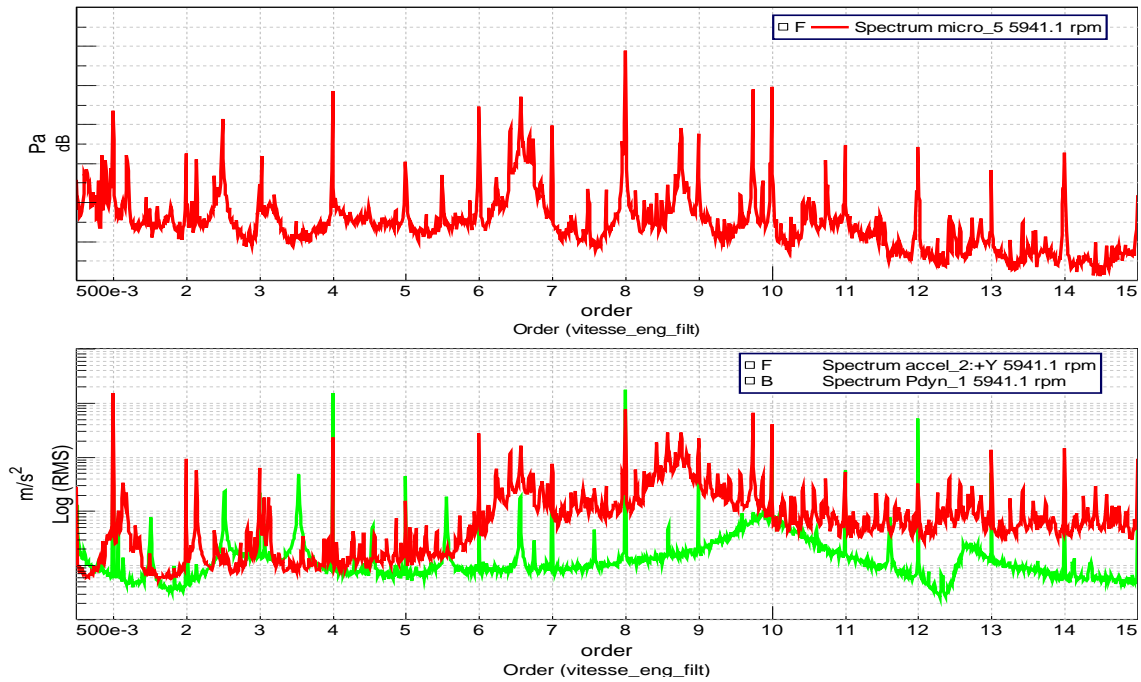


Figure 11: Order spectrum ($\Delta\text{order} = 0.01$); Pump 5
 Top: Microphone 5 (scale: 5 dB/div)
 Bottom: Gear housing accelerometer (red) ; dynamic pressure stage 6 (green)

In the previous figures, the spectral trends of the microphone and accelerometer are similar and seem to indicate that the microphone measures the same phenomenon as the accelerometer. This observation is obvious for Pump 3.

Figure 12 displays the coherence calculated between the gear housing accelerometer and the microphone located 1 m above the pump, for each pump. Obviously, a good coherence is measured for the synchronous phenomena (i.e. related with kinematic frequencies). Nonetheless, a very good coherence is also visible for Pump 3 in the [500 – 1600] Hz and [2200 – 4000] Hz frequency ranges. This type of coherence spectrum is usually representative of a shock response.

Pump 5 also displays good coherence, but in a smaller frequency range: from 600 Hz to 1000 Hz, and between 2500 Hz and 32000 Hz.

Average coherence between the accelerometer and the microphone reaches 0.62 for Pump 3, which is twice as much as the average coherence calculated for Pump 5 and almost 3 times much as that calculated for Pump 1 (see Table 4). The coherence between the microphone and the internal dynamic pressure sensor is only correct for the rotation frequency and its harmonics.

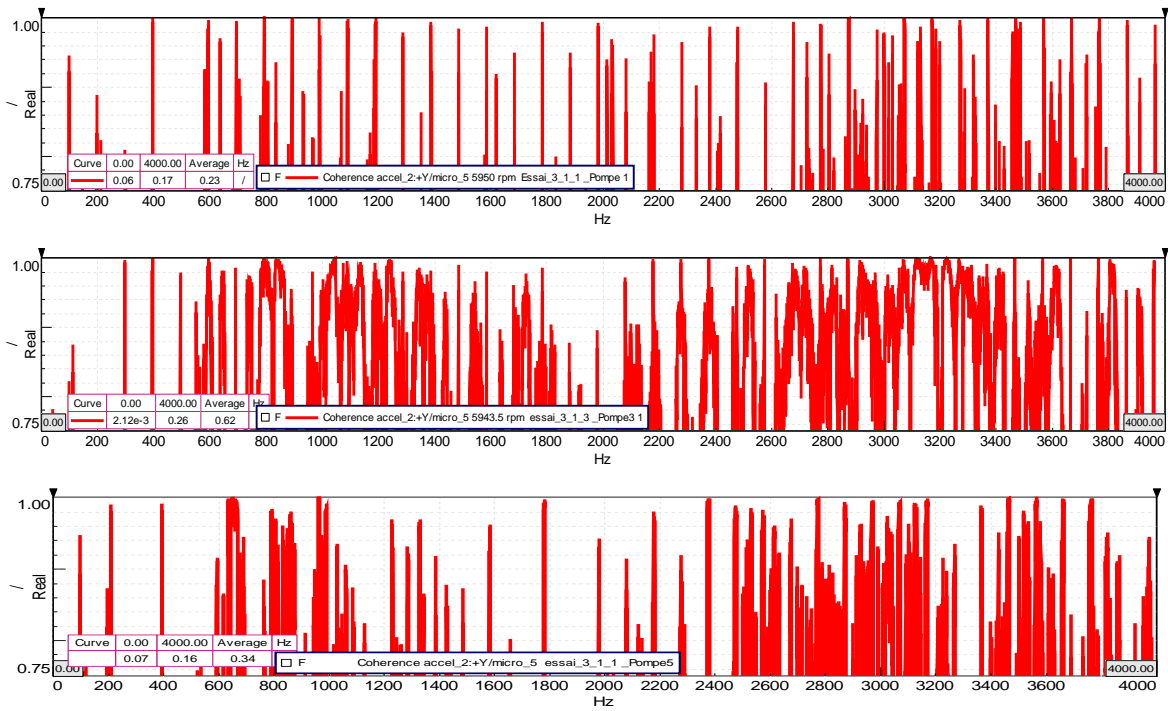


Figure 12: Coherence of the gear housing accelerometer with microphone 5 ($\Delta f = 0.5$ Hz)
 Top: Pump 1 - Middle: Pump 3 - Bottom: Pump 5

	Internal dynamic pressure (exhaust stage)	Gear housing accelerometer
<i>Pump 1</i>	0.09	0.23
<i>Pump 3</i>	0.12	0.62
<i>Pump 5</i>	0.14	0.34

Table 4: Average signal coherences with microphone 5 (frequency range: [0 – 4] kHz)

Considering the unsteadiness perceived during the listening test, the noise and vibration spectral content, and the coherence spectrum which looks like a shock response, a contact loss in the gearing is suspected. This phenomenon is likely to appear, as operating torque and shaft inertia are low, with an important fluid excitation generated on the gear. This assumption was tested in the following section.

3.3 Vibro-impact detection with instantaneous speed measurement – Pump 3

3.3.1 Phenomenon description

As explained before, Pump 3's noise perception differs significantly from the others, as it is unstable and sounds like a rattle noise.

A representative time signal sample recorded on the gear housing accelerometer is plotted in Figure 13. In this signal, from 4.1 s to 4.4 s and from 5.8 s to 6.4 s, a specific event happens: the rattle noise disappeared and the pump noise perception was completely modified. This phenomenon was also perceived on the microphone.

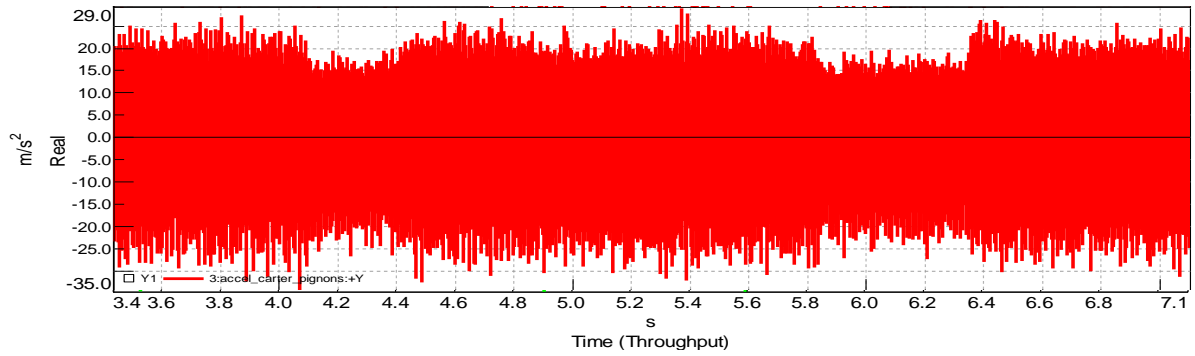


Figure 13: Pump 3 gear housing accelerometer time signal ($F_s = 80 \text{ kHz}$; scale: 5m/s^2)

In order to confirm/infirm the rattle noise phenomenon and the contact loss in the gear, the instantaneous speed of each shaft, or more specifically the instantaneous speed difference between the two shafts, was studied. This instantaneous speed difference is called the relative speed.

3.3.2 Optical encoder data post-processing

The two optical encoders deliver 1000 impulses per revolution, acquired by an 820 MHz acquisition card. The counting method measures the elapsed time between each top (see Figure 14), guaranteeing a good time resolution.

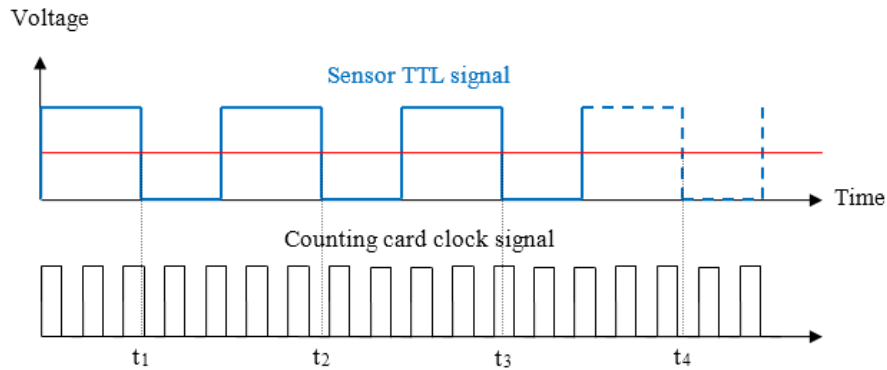


Figure 14: Elapsed time counting method principle

The knowledge of each top time stamp made it possible to determine the angle position vs. time or speed vs. time, relationships plotted Figure 15. The input shaft inertia (in red) is higher than the output shaft's, which can be observed on this figure by less speed fluctuations.

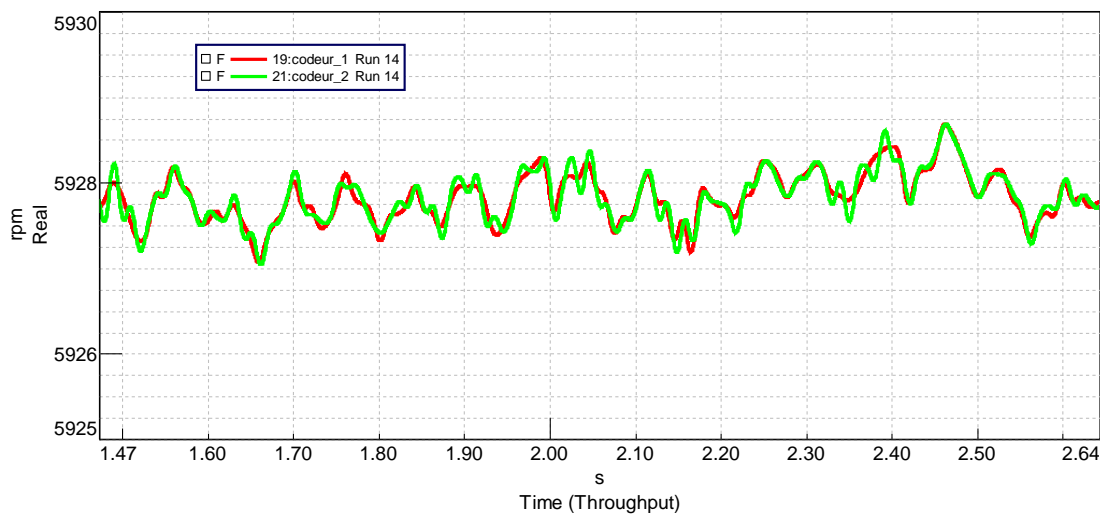


Figure 15: Instantaneous speed vs. time: input shaft (red); output shaft (green)

The rattle phenomenon information is contained in the relative speed signal {input shaft – output shaft} as illustrated hereafter: it is therefore explicit that the signal recorded by the accelerometer is a consequence of what is happening in the gear.

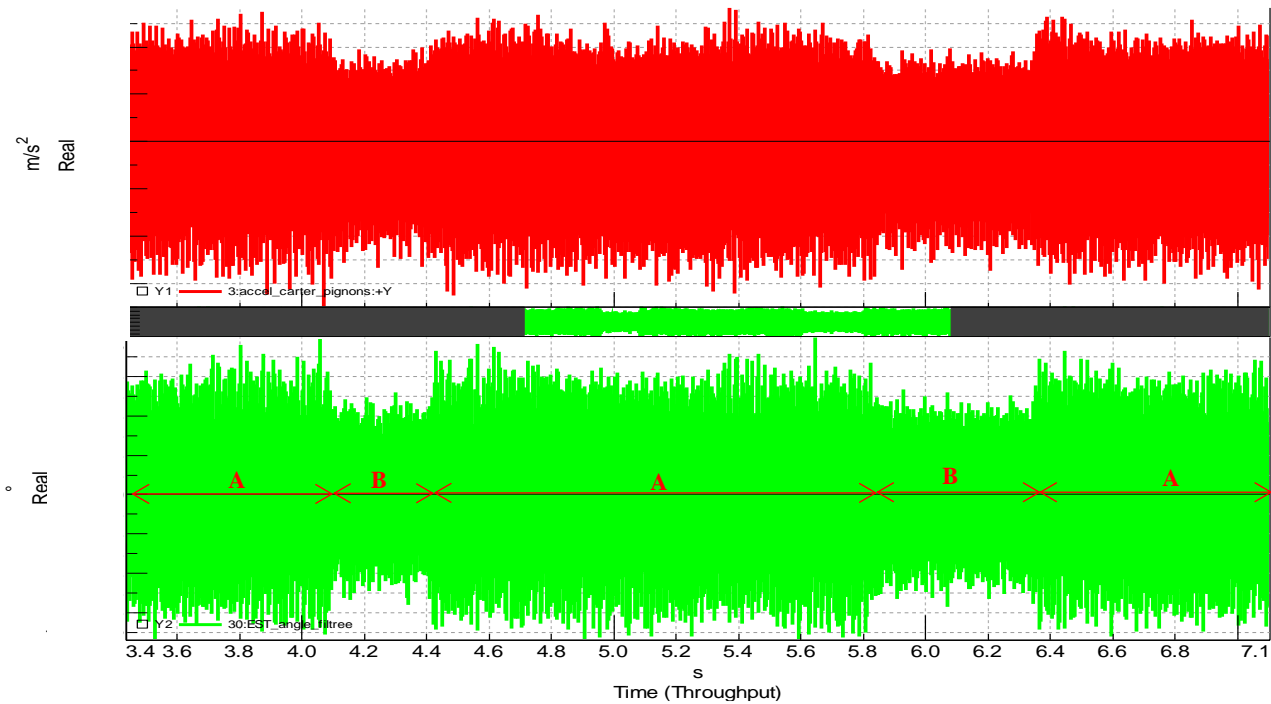


Figure 16: Pump 3 time signal ($F_s = 80 \text{ kHz}$)
 Top: Gear housing accelerometer (scale: 5 m/s^2)
 Bottom: Instantaneous angular position difference (scale: 0.005°)

NB: Figure 16 displays the instantaneous angular position difference ($\Delta\theta$) and not the instantaneous speed difference ($\Delta\dot{\theta}$); Indeed, the latter is more noisy and the rattle phenomenon is more difficult to highlight. Meanwhile, the same information is carried by the angular position and the speed.

3.3.3 Shock detection

A relative speed time sample was plotted in Figure 17. The presence of shocks is obvious. The shock between 1.2234 s and 1.2235 s can be interpreted as follows:

- A: the relative speed decreases, meaning that the output shaft is faster than the input one.
- B: as the output shaft is faster, a shock (B1) occurs between two teeth retro flanks. Consequently, the output shaft is slowed down and become slower than the input shaft (B2): another shock happens (B3).
- C: finally, the output shaft accelerates up to the input shaft speed, and the relative speed tends toward a small value.

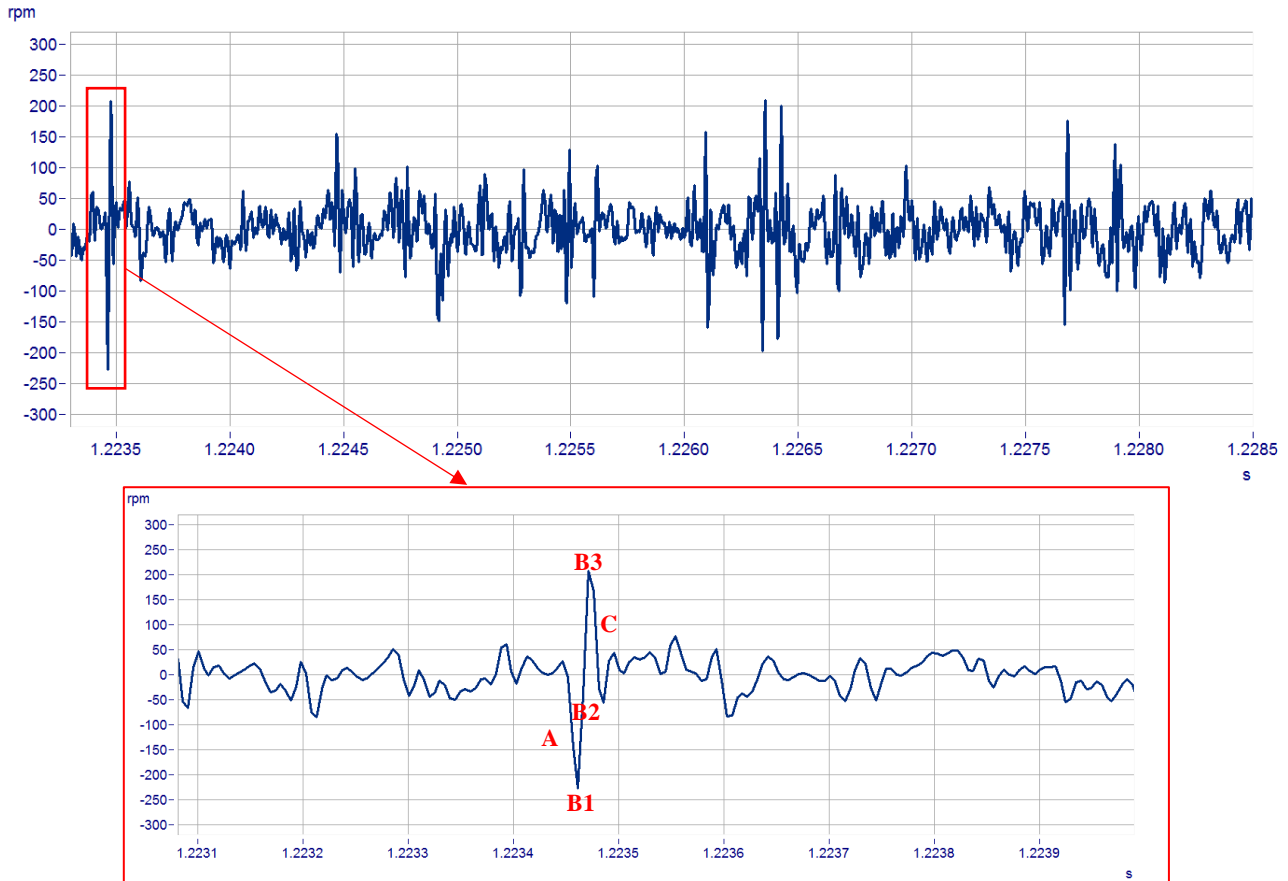


Figure 17: Pump 3 relative speed signal

As the contact loss inside the gear has been highlighted, an assumption can be formulated to explain the phenomenon observed in Figure 16: the noise perception transition may be due to a shift from one vibro-impact regime to another. The nonlinear phenomenon of the contact loss has been studied and described in past years [2], [3], [4], particularly in automotive gearboxes, where the rattle noise is omnipresent [4], [5], [6]. Here, the hypothesis is that Pump 3's operating conditions (temperature, pressure, motor speed, structural dynamic response) position it at the bifurcation close to a period duplication point, leading to two types of vibro-impact response.

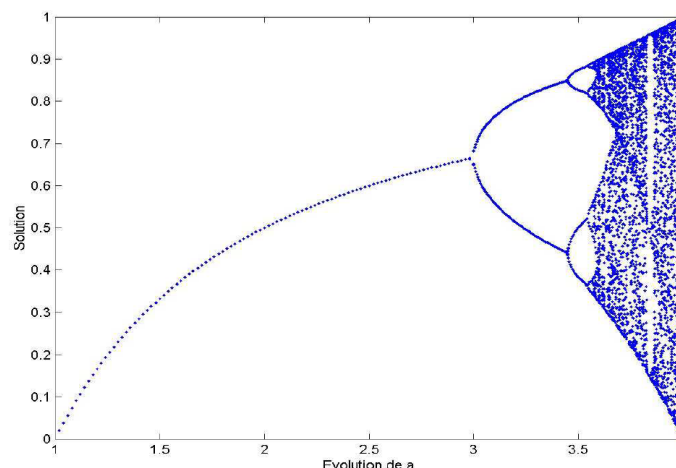


Figure 18: Solution of $x_{n+1} = a x_n (1 - x_n)$ vs. a (source [4])

The work of Kadmiri [6] on automotive gearbox rattle noise is somehow similar to the present study, even though the inertia, speed and excitation are very different. Based on his shock detection method, a threshold was defined to count the shocks on the relative speed signal of the two vibro-impact response types called A

& B, according to the sections plotted on Figure 16. A shock is considered to occur if the relative speed's absolute value exceeds 120 rpm.



Figure 19: Relative speed signal
Top: A-type response; Bottom: B-type response

The shocks were counted for each revolution over a 2 s time sample. The average shock number per revolution is equivalent for both response types: 14.2 (A-type) and 14.3 (B-type).

The counting algorithm made it possible to detect the flank (retro/active) on which the shock occurs and calculate the peak-peak amplitude of each shock. The shock distribution is not really different between the two responses, as illustrated in Table 5.

	Active flank shocks	Retro flank shocks
<i>A-type response</i>	47 %	53 %
<i>B-type response</i>	44 %	56 %

Table 5: Percentage of shocks appearing on the retro / active flanks

However, an amplitude spectrum of the relative speed clearly indicates a behavior difference between the two vibro-impact regimes (Figure 20).

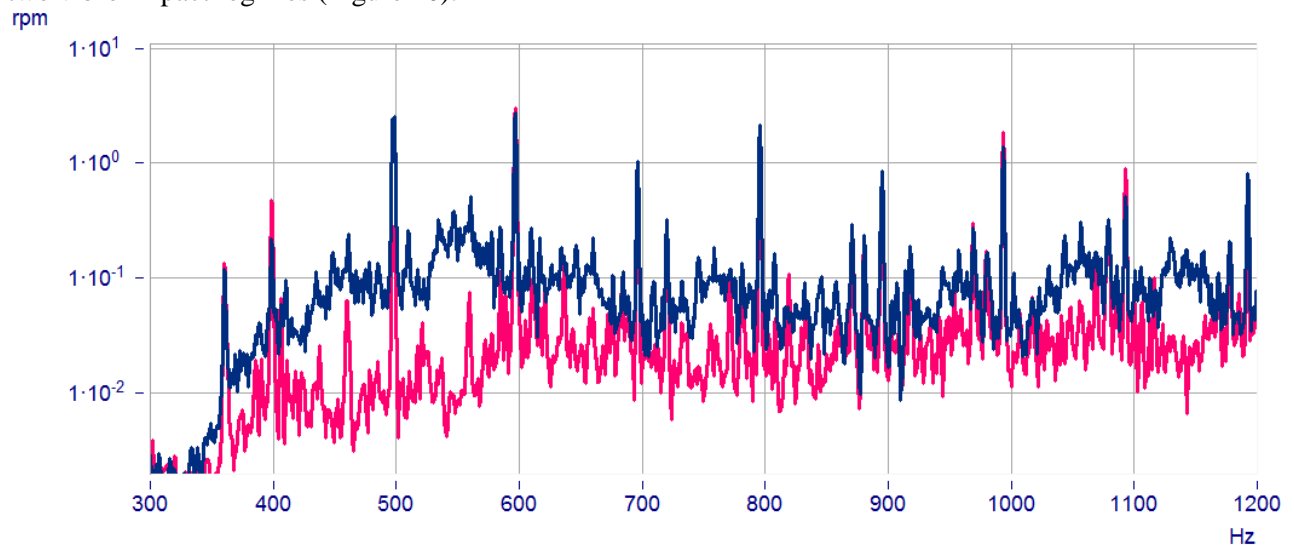


Figure 20: Relative speed amplitude spectra (Δf : 1 Hz) - Blue: A-type response; Red: B-type response

The shock amplitude distribution histogram (Figure 21) indicates some differences between the two response types. In this figure, the retro flank shock amplitudes are negative, while the active flank shock amplitudes are positive.

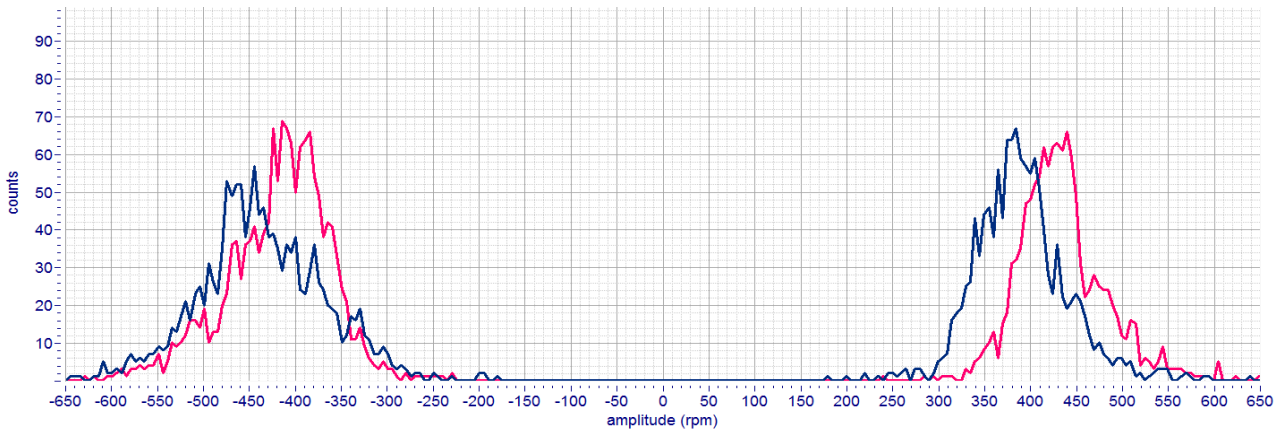


Figure 21: Shock amplitude distribution - Blue: A-type response; Red: B-type response

The B-type histogram is globally symmetrical, as the retro flank and active flank distributions are similar in terms of center value, count and range. On the contrary, the A-type histogram for the retro flank shocks is wider than for the active flank, and centered at -440 rpm, while the active flank part is centered at 370 rpm.

The B-type histogram is more balanced than the A-type, which has a negative average amplitude.

Taking this observation into account, the relative speed's moving mean value was subtracted from the original relative speed signal (Figure 22) and another post-processing was performed.

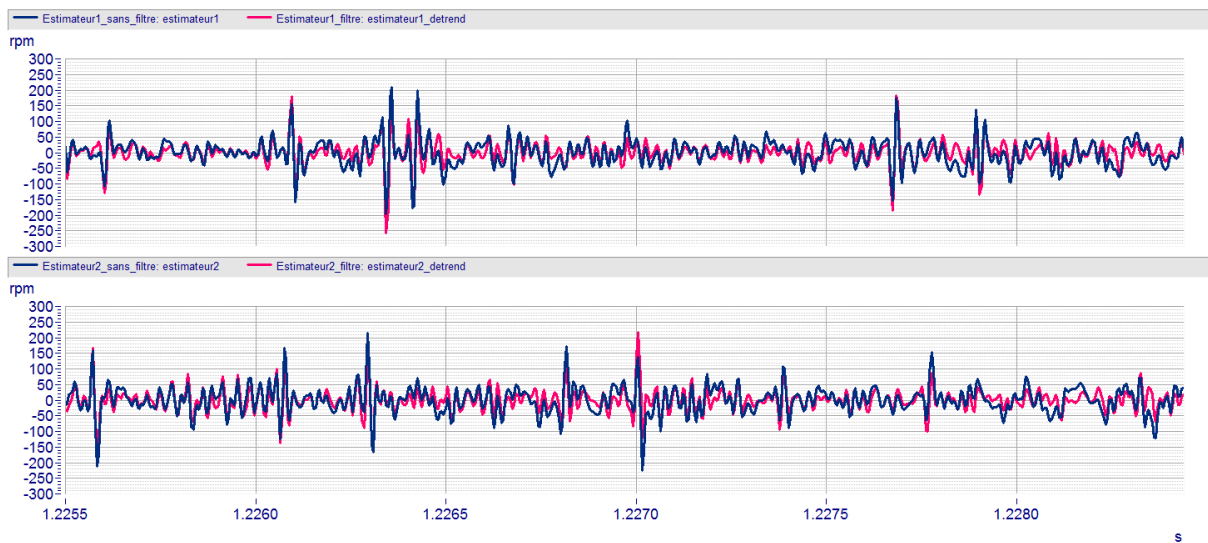


Figure 22: Relative speed signal; Top: A-type response (blue: original; red: moving mean filtered); Bottom: B-type response (blue: original; red: moving mean filtered)

The shock amplitude distribution histogram (Figure 23) compares the results obtained with and without the moving mean value. The B-type response is not significantly impacted by this post-processing.

Inversely, the A-type retro flank shock distribution is completely modified, with the majority of the occurrences in a narrow range centered at an amplitude of 400 rpm. Moreover, the A-type response histogram is clearly asymmetrical.

Finally, it is possible to observe similarities between the A-type response's retro flank shock distribution and the B-type response's active flank shock distribution. At this stage of the project, it is not possible to

conclude with certitude concerning this last assumption, but the shock amplitude distribution histograms clearly highlight two distinct behaviors.

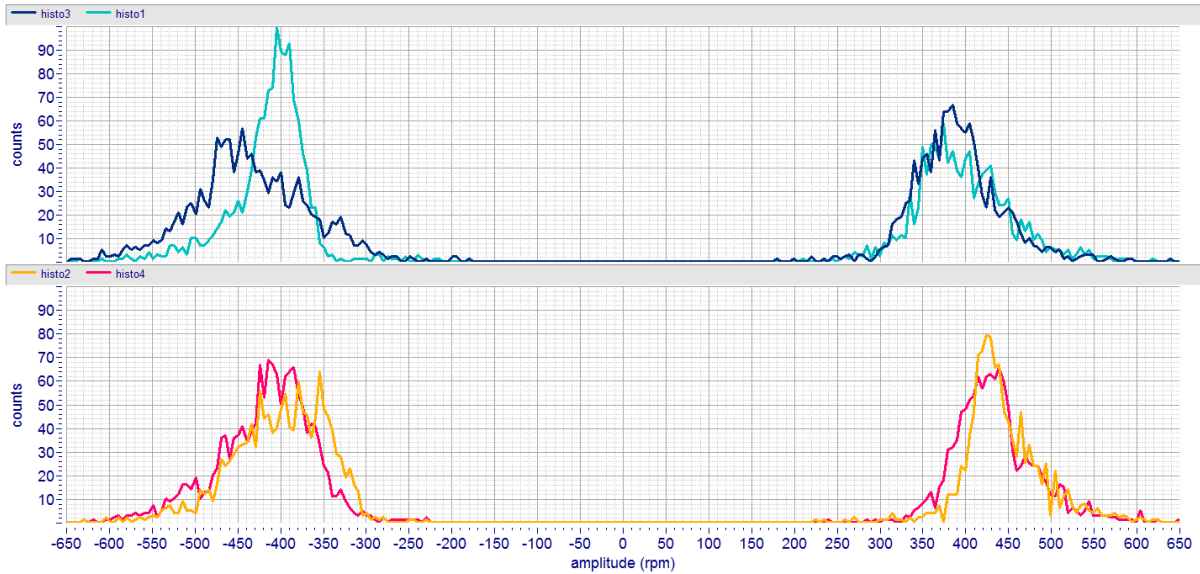


Figure 23: Shock amplitude distribution;
 Top: A-type response - blue; original signal; cyan: filtered signal
 Bottom: B-type response - red; original signal; orange: filtered signal

3.3.4 Combined criterion application

Though a proper explanation of the vibro-impact regime modification has not yet been found, the noise perception between A-type and B-type regimes has been well-identified.

The application of the combined criterion to these two response types is illustrated Figure 24. The vibro-impact regime’s influence is evident on this plot, as the B-type signal is close to Pump 1 in terms of combined criterion and the A-type signal is closer to Pump 5.

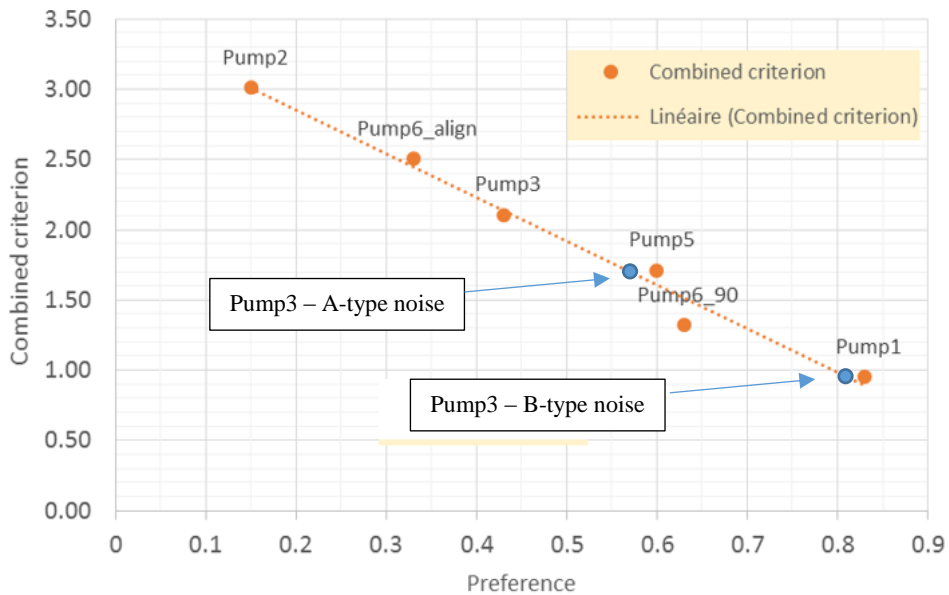


Figure 24: Application of the combined criterion to Pump 3’s different vibro-impact regimes

4 Conclusion

A measurement campaign performed on six different pumps has highlighted significant noise level differences between them, as well as noise perception discrepancies. A psychoacoustic criterion was therefore constructed to sort the pumps.

Among the pumps, three similar specimens exhibit distinct acoustic signatures. The vibroacoustic diagnosis used to compare these pumps has shown that the presence of contact loss in the gear is responsible for the acoustic perception differences. In addition to this, different vibro-impact regimes were identified.

The ARPE project is ongoing and will now focus on identifying the parameters responsible for the vibro impact regime appearance and transitions. The aim is to construct a relationship between these parameters and the psychoacoustic criterion.

5 Acknowledgements

The work presented in this paper has been co-financed by the “European regional development fund” in the framework of the FUI project ARPE.

The authors would like to thank the partners for their help and support during the measurement campaign.

6 References

[1]R. Schicker, G. Wegener, *Measuring Torque Correctly*, HBM publication, pp.18-28.

[2]J. Perret-Liaudet, E. Rigaud, *Response of an Impacting Hertzian Contact to an Order-2 Subharmonic Excitation: Theory and Experiments*. École Centrale de Lyon, France

[3]J. Perret-Liaudet, E. Rigaud, *Experiments and Numerical Results on Nonlinear Vibrations of an Impacting Hertzian Contact*. École Centrale de Lyon, France

[4]T. Amado, *Modélisation d'un système dynamique à jeu du groupe moto-propulseur*, Phd thesis, École Centrale de Lyon, France, 2006.

[5]A. Carbonelli, *Caractérisation vibro-acoustique d'une cascade de distribution poids lourd*, Phd thesis, École Centrale de Lyon, France, 2012.

[6]Y. Kadmiri, *Analyse vibroacoustique du bruit de grailonnement des boîtes de vitesses automobiles*. Phd thesis, École Centrale de Lyon, France, 2011.